ADVANCED FUNCTIONAL MATERIALS
www.afm-journal.de

Organic Surface Doping for High-Performance Perovskite Transistors

*Ju-Hyeon Kim, Chang-Mok Oh, In-Wook Hwang, Kiyoung Park, and Kwanghee Lee**

Quasi-2D perovskites have attracted significant attention because of their environmental robustness and superior long-term stability compared with their 3D counterparts. However, they typically consist of a mixture of multiple quantum wells with different optoelectrical properties, which degrades the electronic properties and hinders further electronic applications. Here, to challenge this issue, a surface p-doping strategy involving the introduction of a thiophene-containing polymer onto the surface of quasi-2D tin perovskites is reported. The tin ions in the perovskites effectively interact with the sulfur atoms in the thiophene moieties, thereby generating hole carriers and inducing p-doping. The resulting doped quasi-2D perovskites exhibit excellent surface crystallinity, lower trap density, and enhanced charge carrier transport capability along the perovskite semiconductor channels. Consequently, the doped quasi-2D tin perovskite-based transistors exhibit a high field-effect mobility of 53 $cm^2V^{-1}s^{-1}$ (7 $cm^2V^{-1}s^{-1}$ for the control device) and an outstanding on/off ratio (>10^7), together with superior operational stability.

1. Introduction

Metal halide perovskites have emerged as highly promising semiconductors for next-generation electronic applications, including monolithic 3D integration, neuromorphic devices, and single quantum sensors/emitters, benefiting from their easy processing and high carrier mobilities.[1–3] Thin-film transistors (TFTs) based on 3D tin (Sn) perovskites, which are generally described as having a stoichiometry of $ASnX_3$, where A represents an organic or inorganic monovalent cation (such as formamidinium, FA^+, or cesium, Cs^+) and X denotes a halide anion, exhibit excellent p-type semiconductor properties owing to their low hole carrier effective mass and defect-tolerant.[4–6] The p-type nature of 3D tin perovskites originates from strong tin-halide orbital coupling near the valence band edge (VBE), which generates Sn vacancies (V_{Sn}) that act as a source of hole carriers.[7–9] Despite their excellent p-type properties, 3D tin perovskites are easily oxidized in an air atmosphere, thereby significantly deteriorating their transport properties and limiting their device applications for further commercialization.[10]

2D Ruddlesden-Popper perovskites (RPPs) with the tin-based formula $(A')_2SnX_4$, where A´is a bulky organic cation (e.g., phenethylammonium, PEA^+), exhibit distinctive optoelectrical properties.[11–13] The bulky organic cations are positioned within an inorganic $[SnX_6]^{4-}$ octahedral framework and form quantum wells (QWs).[14] This unique structure contributes to the superior environmental stability of 2D RPPs because the hydrophobic nature of the bulky organic cations protects the perovskite from external contaminants such as oxygen and moisture.[15] However, due to the intrinsically insulating properties of bulky organic cations, the field-effect mobility (μ_{FE}) of the solution-processed RPP-based TFTs (<5 $cm^2V^{-1}s^{-1}$) is quite low compared with that of 3D perovskites (>50 $cm^2V^{-1}s^{-1}$).[16,17] The strategy of hybridizing 2D and 3D perovskites, with the resulting materials generally referred to as quasi-2D perovskites, provides another approach. These quasi-2D perovskites combine the advantages of 2D (environmental stability) and 3D (high field-effect mobility) perovskites.[18] Despite the improved properties of quasi-2D perovskites, they still suffer from an inhomogeneous crystal distribution with a mixture of multiple QWs, which hinders efficient current flow through semiconductor channels.[19,20] This situation greatly degrades their electrical properties and hinders their further electronic applications.[21]

Electronic doping with substitutional impurities is one of the most powerful techniques for controlling the electronic properties of conventional silicon-based semiconductors, thereby advancing semiconductor physics and modern microelectronics.[22–25] However, regulating the electronic properties of perovskites via a similar systematic approach is

J.-H. Kim, K. Lee
Heeger Center for Advanced Materials (HCAM)
Gwangju Institute of Science and Technology (GIST)
Gwangju 61005, Republic of Korea
E-mail: klee@gist.ac.kr
C.-M. Oh, I.-W. Hwang
Advanced Photonics Research Institute
Gwangju Institute of Science and Technology (GIST)
Gwangju 61005, Republic of Korea
K. Park, K. Lee
School of Materials Science and Engineering
Gwangju Institute of Science and Technology (GIST)
Gwangju 61005, Republic of Korea
The ORCID identification number(s) for the author(s) of this article can be found under https://doi.org/10.1002/adfm.202411836

DOI: 10.1002/adfm.202411836

challenging because of their intrinsic defects, which exhibit strong charge-compensating behavior.[26,27] Recent attempts at organic modification of 3D perovskites have demonstrated the potential for electronic tuning of these perovskites.[28,29] Similar to electronic doping, the integration of organic moieties strongly influences the electronic structure of perovskites, enabling fine-tuning of the charge carrier density and mobility. Nonetheless, exploiting the interactions between organic moieties and perovskites for practical applications has not been explored in detail.

Here, to enhance the electronic properties of quasi-2D perovskites, we introduce a new doping strategy involving polymer modification on their top surface. This organic molecular surface doping strategy suppresses trap-assisted recombination and, consequently, leads to efficient charge carrier transport, based on transient absorption spectroscopy analysis. Leveraging these benefits, efficient p-type quasi-2D perovskite-based TFTs (quasi-2D TFTs) with a high μ_{FE} of 53 $cm^2V^{-1}s^{-1}$(7 $cm^2V^{-1}s^{-1}$ for the control device), an excellent on/off ratio (I_{on}/I_{off}) of 2.36×10^7, and superior operational stability, are attained. Our work advances the fundamental understanding of the surface molecular doping physics of quasi-2D perovskites and their charge transport dynamics for novel optoelectronic applications.

2. Results and Discussion

2.1. Surface Modification Strategy and Electrical Property Analysis

We used a low-dimensional tin-based quasi-2D perovskite material, $\eta = 7$ $(PEA)_2(FA)_6Sn_7I_{22}$ (where η represents the width of the inorganic perovskite) with multiple η values ($\eta \leq 7$), because it exhibited both 2D and 3D perovskite properties (**Figure 1a**). To investigate the effects of polymer modification of quasi-2D perovskites, we selected different types of representative polymer materials, including the nonconjugated polymer polystyrene (PS), the conjugated homopolymer poly(3-hexylthiophene) (P3HT), and the conjugated copolymer poly[2,5-(2-octyldodecyl)−3,6-diketopyrrolopyrrole-alt-5,5-(2,5-di(thien-2-yl)thieno[3,2-b]thiophene)] (TT); their chemical structures are depicted on the right side of Figure 1a. In an endeavor to investigate the chemical interaction between the quasi-2D perovskite and polymers, we performed X-ray photoelectron spectroscopy (XPS) measurements on the control and each polymer-modified thin film. All samples were prepared via low-temperature solution processing, and the thicknesses of the thin films were measured to be <40 nm by a surface profiler: ≈30 nm for the control perovskite and ≈35 nm for the polymer-modified samples. In the XPS spectrum of the control film (Figure 1b), we observed distinct peaks corresponding to the binding energies of Sn $3d_{3/2}$ (494.08 eV) and Sn $3d_{5/2}$ (485.68 eV), and these peaks shifted to lower binding energies after polymer modification. More importantly, two additional peaks for tetravalent tin (Sn^{4+}) were observed in the spectra of the thiophene-containing polymer (P3HT and TT)-modified samples, which originated from Sn-S interactions, as determined by Fourier transform infrared (FTIR) spectroscopy (Figure 1f,g).[30,31] The C-S vibration-related peak (1260 cm^{-1}) of the thiophene group slightly shifted and broadened upon interaction with the Sn ions of the perovskite.

To estimate the relative abundance of the two oxidation states, we calculated the peak area ratio $A_{Sn^{4+}}/A_{Sn^{All}}$, where $A_{Sn^{4+}}$ represents the area of the Sn^{4+}-related peaks (orange regions) and $A_{Sn^{All}}$ denotes the area of the entire Sn spectrum. The proportions of Sn^{4+} in the thiophene-containing polymer-modified samples were 24.09% (with P3HT) and 28.63% (with TT). The difference between these values indicated that the TT polymer interacted more effectively with the Sn ions on the perovskite surface because of the weaker steric hindrance effect from thiophene (Figure S1, Supporting Information). The formation of Sn-S interactions led to a decrease in the electron density of the Sn—I bonds, resulting in the formation of I_2 or I_3^- ions on the perovskite surface, as confirmed by the iodine 3d spectra (Figure 1c).[10,32–35] Furthermore, the deconvolution of the S 2p binding energy peaks strongly supported the occurrence of Sn-S interactions. The proportion of S_2^{2-} or S_n^{2-} ions increased from 12.41% to 14.79% (with P3HT, Figure 1d) and from 8.87% to 14.65% (with TT, Figure 1e).[36,37] This change in the proportion was due to the electron-accepting nature of the sulfur atoms in the thiophene units, which accepted electrons from the tin ions. Typically, oxidation of divalent tin (Sn^{2+}) ions to Sn^{4+} in tin perovskites induces lattice instability, and Sn^{4+} acts as a defect-mediated recombination center since Sn^{4+} ions are incorporated into the perovskite lattice. To assess the incorporation of Sn^{4+} resulting from Sn-S interactions in perovskite materials, we obtained XPS depth profiles (Figure S2, Supporting Information) and corresponding Sn 3d spectra (Figure S3, Supporting Information). Sn^{4+} ions only existed in the thiophene-containing polymer samples and were confirmed to be found only at the top surface of the perovskite films. These results indicated that the polymer modification strategy did not affect the lattice instability of the perovskite films, which was induced by Sn^{4+} incorporation.

To elucidate the electronic structure of the quasi-2D perovskites, we conducted ultraviolet-visible (UV-Vis) absorption spectroscopy (Figure S4, Supporting Information) and UV photoelectron spectroscopy (UPS, Figure S5, Supporting Information) measurements, from which the bandgap, Fermi energy level (E_F), and valence band maximum (VBM) of the perovskite materials could be determined. **Figure 2a** presents the corresponding energy level diagrams of the control and each polymer-modified quasi-2D perovskite film. Owing to the Sn-S interaction, E_F shifted toward the VBM: the E_F values were −4.47 eV (control), −4.55 eV (with PS), −4.65 eV (with P3HT), and −4.79 eV (with TT), and the shift originated from the generation of Sn^{4+} and V_{Sn} at the VBE. Moreover, as depicted in Figure 2b, we further performed Hall effect measurements to evaluate the electrical properties of the quasi-2D perovskite films. The control film exhibited an average hole carrier density of 6.44×10^{15} cm^{-3} and an average Hall mobility (μ_{Hall}) of 42 $cm^2V^{-1}s^{-1}$. Furthermore, the PS-modified samples had slightly increased hole carrier density (7.28×10^{15} cm^{-3}) and μ_{Hall} (61 $cm^2V^{-1}s^{-1}$), which were related to the defect passivation effect of the PS material. Notably, the perovskite films modified with the thiophene-containing polymers exhibited a significant increase in the hole carrier density (1.07×10^{16} cm^{-3} for the sample with P3HT and 2.36×10^{16} cm^{-3} for the sample with TT) and excellent μ_{Hall} values of 113 $cm^2V^{-1}s^{-1}$ (with P3HT) and 136 $cm^2V^{-1}s^{-1}$ (with TT), respectively. Therefore, based on these chemical and electrical property analysis results, the S atom in the thiophene unit could interact with the

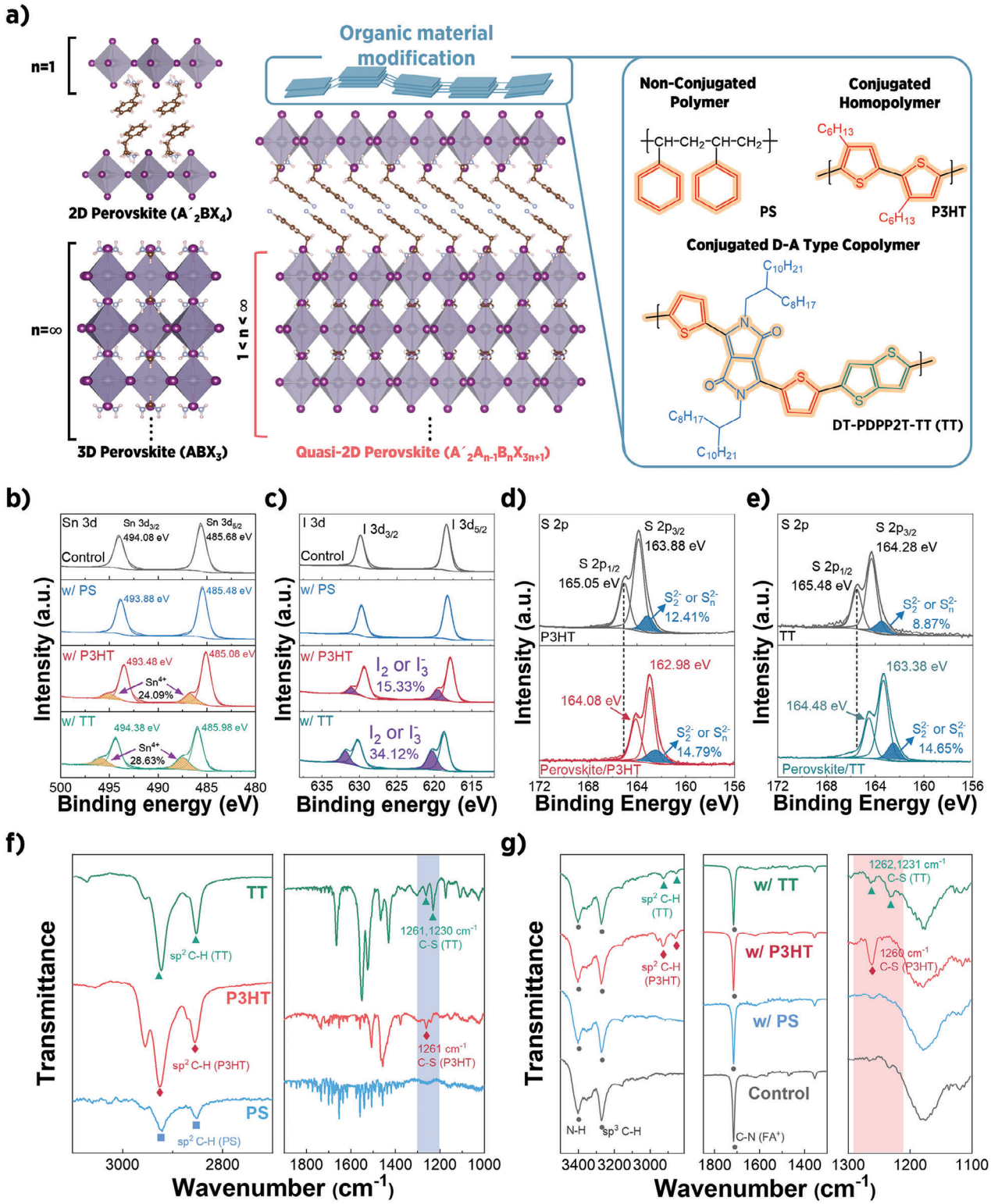

Figure 1. Perovskite top surface modification. a) Schematic illustration of the polymer modification strategy, corresponding quasi-2D perovskite, and representative polymer materials. High-resolution XPS analysis of each quasi-2D perovskite thin film. b) Sn 3d and c) I 3d core-level spectra of the control (black) and the samples with PS (blue), P3HT (red), and TT (green). The orange and purple regions correspond to Sn^{4+} and I_3^- (or I_2), respectively, as determined from the area under the corresponding curve. S 2p spectra of d) P3HT and e) TT: homopolymer film (black), P3HT-modified quasi-2D perovskite (red), and TT-modified quasi-2D perovskite (green). The corresponding blue regions are S_2^{2-} or S_n^{2-}. FTIR spectra of f) each homopolymer film and g) modified quasi-2D perovskite films: control (black), with PS (blue), with P3HT (red), and with TT (green). The C-S-related vibration peak in the samples is shown in the blue and red regions.

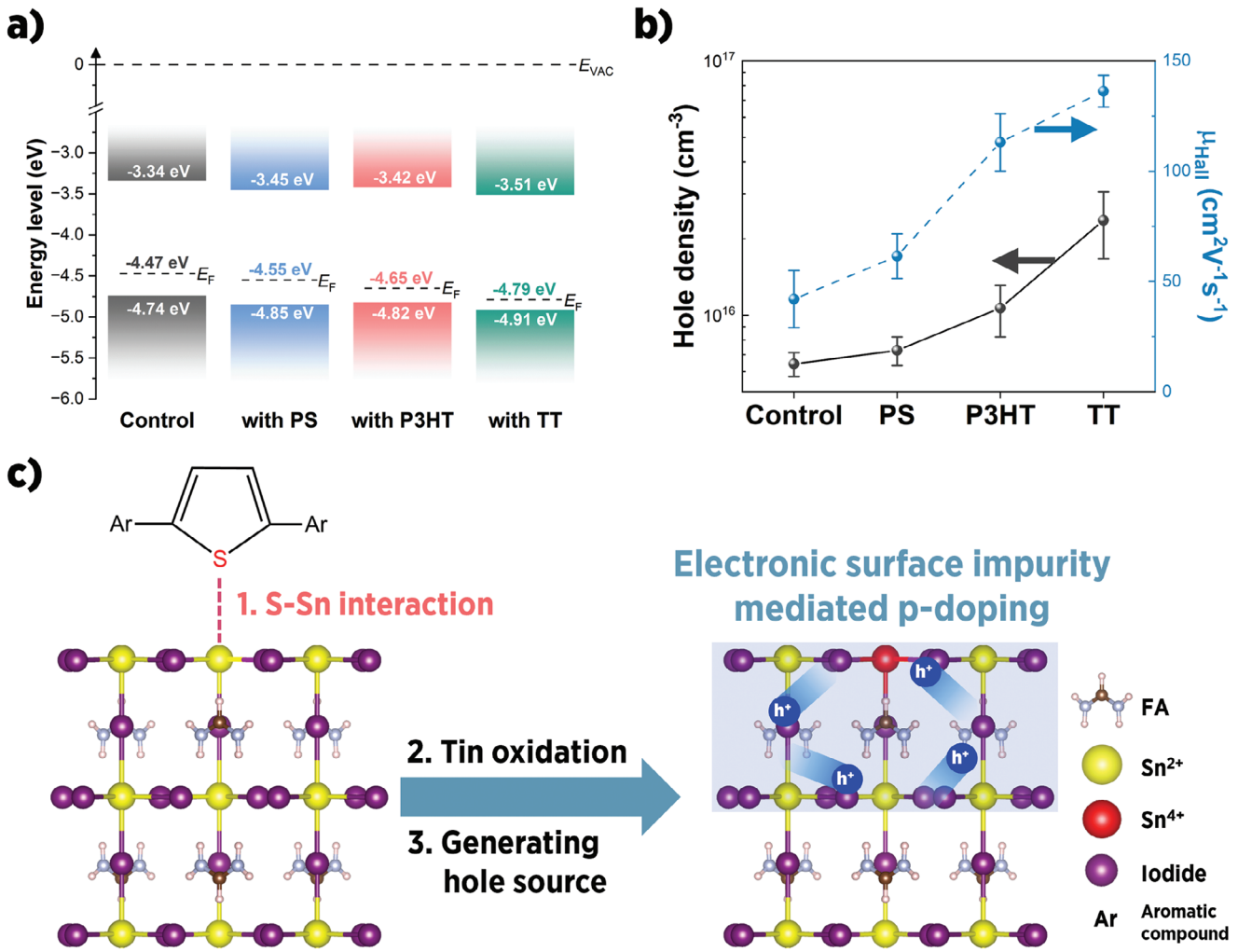

Figure 2. Surface impurity-mediated p-doping strategy. a) Schematic representation of the energy level diagrams of each quasi-2D perovskite material. E_F and E_{VAC} represent the energies of the Fermi and vacuum levels, respectively. b) Hall effect measurement results of each quasi-2D perovskite thin film, showing the corresponding hole carrier density (left axis) and Hall mobility (right axis). Error bars were calculated from the individual measurements of fifteen samples. c). Schematic illustration of the surface molecular p-doping strategy involving molecular-level interactions between the tin atoms of the perovskite and the sulfur atoms in the thiophene unit of the polymer materials.

surface Sn ions, leading to the oxidation of Sn^{2+} to Sn^{4+}, which generated hole carriers at the surface of the quasi-2D perovskite and induced p-doping (Figure S6, Supporting Information). We denote this strategy as "electronic surface impurity-mediated p-doping" (Figure 2c), and this novel p-doping strategy improves the electrical properties of perovskite materials, which is expected to enhance their TFT performance.

2.2. Physical and Optical Characterization

To observe the changes in the morphology of the quasi-2D perovskites modified with various polymers, we conducted scanning electron microscopy (SEM, Figure S7, Supporting Information) and atomic force microscopy (AFM, Figure S8, Supporting Information) analyses. The values of root-mean-square (RMS) and surface area notably decreased in the polymer-modified films (detailed values of the surface area are included in Table S1, Supporting Information). The smooth morphology of the perovskites could contribute to a homogeneous electric field in TFT applications, leading to increased TFT performance.[38] Furthermore, to determine how polymer modification influences the crystallography of the perovskite, grazing-incidence X-ray diffraction (GIXRD) studies were carried out on each quasi-2D perovskite thin film at various incidence angles (Figure S9, Supporting Information). All the samples exhibited peaks corresponding to both 3D perovskites, such as the (110) and (220) planes, and 2D perovskites, including the (020) and (004) planes; thus, these samples were quasi-2D perovskite materials (**Figure 3a**).[39,40] Moreover, we collected the full width at half maximum (FWHM) of the peak corresponding to the perovskite (110) plane at 2θ = 14.0°. As shown in Figure 3b, the polymer-modified samples had lower FWHM values at an incidence angle of 0.1°, and the sample with TT had the narrowest FWHM. These results indicated that polymer modification increased the surface crystallinity of the quasi-2D perovskites.

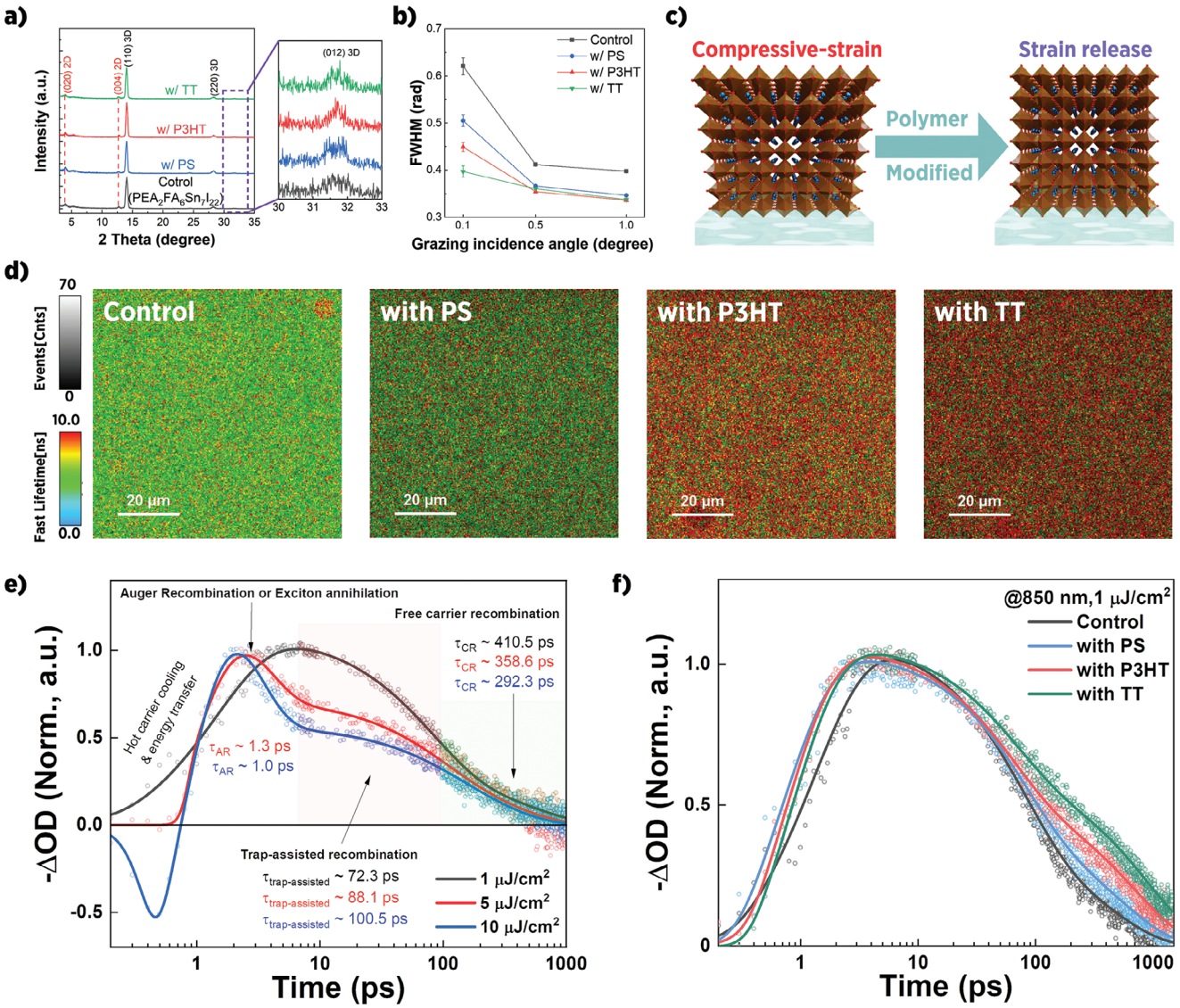

Figure 3. Physical and optical characterization of the quasi-2D perovskite materials. a) GIXRD patterns of each quasi-2D perovskite film, corresponding to the perovskite (012) plane (right side), and b) incidence angle dependence of the FWHM of the peak corresponding to the quasi-2D perovskite (110) plane – control (black) and samples with PS (blue), P3HT (red), and TT (green). c) Schematic illustration of the lattice structure: compressive strain (left) and strain release effect of the polymer modification (right). d) Average lifetime mapping images of the control quasi-2D perovskite film and films with PS, P3HT, and TT. The color scale bar indicates the average fast decay carrier lifetime, whereas the grayscale bar indicates the event count. e) Power dependence analysis of the TA spectrum of the control quasi-2D perovskite film (signal at 820 nm). Corresponding laser powers: 1 (black), 5 (red), and 10 (blue) μJ·cm^{-2}. f) Kinetics extracted from the TA signals at 850 nm for the control quasi-2D perovskite (black) and samples with PS (blue), P3HT (red), and TT (green).

To collect strain information for the perovskite crystals, we calculated the incidence angle dependence of the lattice d-spacing of the perovskite (012) plane (right side of Figure 3a; Figure S10, Supporting Information).[41] The d-spacing monotonically increased with increasing incidence angle for all the perovskite samples, indicating that the compressive strain within the perovskite materials caused additional defects and consequently undesirable nonradiative recombination processes.[42] However, the slopes of the samples modified with the thiophene-containing polymers (P3HT and TT) were lower than those of the control and PS-modified samples. This result implied that the thiophene-containing polymer modification strategy induced strain release in the perovskite materials (Figure 3c). Therefore, based on these crystallographic analysis results, polymer modification effectively increased the surface crystallinity and reduced the strain of the perovskite crystals, which could induce efficient charge transport in the quasi-2D perovskite materials.

Considering the possible influence of Sn-S interaction-mediated surface molecular p-doping on the optical and photophysical properties of quasi-2D perovskites, we performed photoluminescence (PL) analysis and time-resolved spectroscopy measurements of the quasi-2D perovskite thin films. As shown in

Table 1. TA parameters of each quasi-2D perovskite sample.

Probe[a] wavelength [nm]	Sample	Fitted time constants[b] [ps]			
		τ_1^{TA}	τ_2^{TA}	τ_3^{TA}	τ_{avg}^{TA}
850	Control	1.4 rise	72.3 (69%)	410.5 (31%)	177.1
	with PS	0.7 rise	69.7 (60%)	550.7 (40%)	262.1
	with P3HT	0.7 rise	67.7 (51%)	710.3 (49%)	382.5
	with TT	0.7 rise	69.9 (44%)	910.7 (56%)	540.7

[a] To prohibit the oxidation of tin-based perovskite materials, all samples were encapsulated with cover glass; and [b] The decay curves were fitted with a biexponential decay model after the rise time (τ_1): $\Delta OD(t) = A_2 \exp(-t/\tau_2) + A_3 \exp(-t/\tau_3)$, where $\Delta OD(t)$ is the time-dependent TA intensity, A is the amplitude (noted in parentheses as the normalized percentage, i.e., $[A_i/(A_2 + A_3)] \times 100$), and τ is the decay time.

Figure S11 (Supporting Information), the PL spectra exhibited a blueshift and broadening; the wavelengths corresponding to the PL maximum (λ_{PL}^{max}) were 870.6 nm (control), 866.9 nm (with PS), 866.1 nm (with P3HT), and 861.0 nm (with TT). This phenomenon was caused by surface p-doping, which was induced by the increase in the hole carrier density at the VBE originating from the process.[43] The increased population of states near the VBE resulted in a higher probability of radiative recombination. Further, the reduced compressive strain of the perovskite materials affected their band structures, leading to a blueshift.[42,44] Furthermore, p-doping could improve the scattering processes, facilitating energy exchange between the carriers and lattice vibrations, which broadened the emission. The PL analysis provided strong support for the p-doping of the quasi-2D perovskites via Sn-S interactions and was consistent with the results of the UPS and Hall effect measurements.

The average carrier lifetime mapping images are shown in Figure 3d. The light-green region with a relatively short lifetime (control quasi-2D perovskite) gradually transitioned to the green (with PS), red (with P3HT), and deep red (with TT) regions with an increase in the lifetime. The detailed time-resolved PL (TRPL) decay curve and its time parameters are depicted in Figure S12 and Table S2 (Supporting Information). The TRPL decay profiles were fitted with a biexponential function; the fast decay component (τ_1) was related to nonradiative recombination induced by trap states of perovskites, whereas the relatively slow decay component (τ_2) was assigned to the bimolecular recombination process.[45] After the quasi-2D perovskite was modified with the polymers, the value and proportion of τ_1 decreased because of the trap passivation effect of the polymers. In addition, the corresponding value and proportion of τ_2 increased; thus, the increased radiative recombination was caused by the doped hole carriers produced by the surface molecular p-doping, which is similar to electronic doping in conventional inorganic semiconductors.

To gain a deeper understanding of the carrier recombination dynamics of the quasi-2D perovskites, we conducted picosecond transient absorption (ps-TA) analyses on the control quasi-2D film and each polymer-modified film. First, we measured the power dependence of the ps-TA spectrum of the control quasi-2D perovskite to optimize the laser power and confirm the recombination process (Figure 3e). As the laser power increased from 1 to 5 and 10 μJcm^{-2}, a specific shoulder curve appeared at <2.0 ps; this peak was related to Auger recombination or exciton annihilation due to the increase in the number of charge carriers in the quasi-2D perovskites with a higher laser power. Furthermore, trap-assisted recombination (red regions) and free carrier recombination regions (green regions) were also observed in the sub-100 ps and over-100 ps regimes, respectively. Therefore, we used a laser power of 1 μJcm^{-2} to exclude the Auger recombination process caused by an excessive charge carrier density. As shown in Figure S13 (Supporting Information), all the ps-TA spectra showed photobleaching (PB, at 510 and 600 nm) and photoinduced absorption (PIA, at 550 and 670 nm) peaks because the quasi-2D perovskites had multiple QWs with different η values. The PB signals at 850 nm originate from 3D perovskite-like behavior in quasi-2D perovskite, which serves as the main transport channel of quasi-2D TFTs. The corresponding PB (at 850 nm) decay curves for all the samples are shown in Figure 3f, and the detailed decay times are summarized in **Table 1**.[46] The PB rise time (τ_1^{TA}) was different between the control sample and polymer-modified samples, and this difference was related to the surface crystallinity changes and strain release in the polymer-modified samples, as discussed in relation to Figure 3c, which led to different lattice vibrations and carrier relaxations. Furthermore, the polymer-modified samples had a relatively low proportion of the sub-100 ps decay time (τ_2^{TA}) and a simultaneously high proportion of the above-100 ps decay time (τ_3^{TA}). These results indicated suppressed trap-assisted recombination and increased free charge carrier radiative recombination in the polymer-modified quasi-2D perovskites. In particular, the sample with TT had the longest τ_3^{TA} of 910.7 ps and a τ_{avg}^{TA} of 540.7 ps (410.5 ps and 177.1 ps for the control sample, respectively); these results provide evidence of efficient charge carrier transport in the perovskite materials.

2.3. Characterization of the TFT Performance

We applied our novel electronic surface impurity-mediated p-doping strategy to practical TFT applications. In this study, we adopted the following top-contact bottom-gate quasi-2D TFT configuration: Si/SiO_2/quasi-2D perovskite/optional polymer layer/gold (Au), as illustrated in **Figure 4a**. The optimized polymer modification conditions are shown in Figure S14 (Supporting Information). To clarify the uniformity of the polymer modification of the quasi-2D perovskites, high-resolution transmission electron microscopy (HRTEM) analysis was performed on the quasi-2D TFTs, as shown in Figure 4b, and these results were consistent with the TFT device structure depicted in Figure 4a. For a more detailed examination of the interface

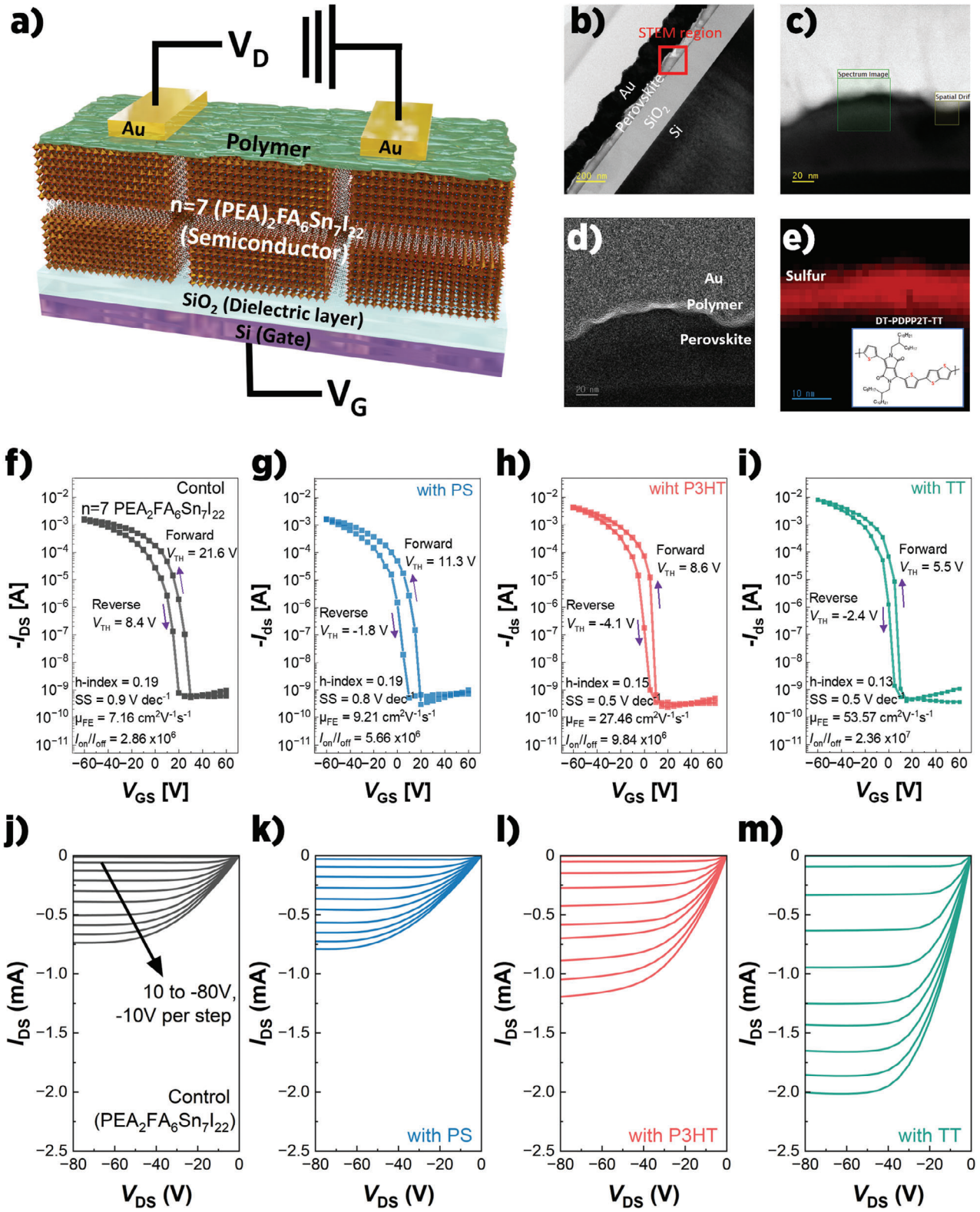

Figure 4. TFT structure and device performance characterization. a) Schematic of the quasi-2D perovskite [$(PEA)_2FA_6Sn_7I_{22}$]-based TFT (quasi-2D TFT) device structure. The device configuration consists of a top-contact bottom-gate system with Si (gate electrode)/SiO_2 (dielectric layer)/quasi-2D perovskite (semiconductor layer)/optional polymer material/Au (source and drain electrodes). b) Cross-sectional HRTEM image of a quasi-2D TFT with the TT polymer (concentration of 4.0 mg mL^{-1}): Si/SiO_2/quasi-2D perovskite/TT polymer/Au. c), HAADF-STEM image of the interface between

between the quasi-2D perovskite and polymers, we analyzed high-angle annular dark-field scanning TEM (HAADF-STEM) images of the red rectangular regions (Figure 4c) and performed Sobel processing (Figure 4d; Figure S15, Supporting Information), which is a digital image processing method used to detect and identify boundaries in images.[47] The processed image revealed that the polymer materials were uniformly distributed between the perovskite and gold layers. Furthermore, to identify and cross-check the polymer materials, we performed sulfur atom mapping via electron energy loss spectroscopy (EELS) in the green region (Figure 4e). Sulfur atoms from the thiophene unit of the TT polymer were observed on the top surface of the perovskite. These TEM analyses indicated that the polymer materials were uniformly present on the top surface of the perovskite material and did not interact with the bulk perovskite films, effectively agreeing with the XPS depth profile analysis.

The transfer curves of the optimized quasi-2D TFTs without or with each polymer material are presented in Figure 4f–i. The control device exhibited a typical quasi-2D TFT performance with a μ_{FE} of 7 $cm^2V^{-1}s^{-1}$ (average μ_{FE} ≈6.45 ± 0.53 $cm^2V^{-1}s^{-1}$, Figure S16, Supporting Information), an I_{on}/I_{off} of 2.86 × 10^6, and a threshold voltage (V_{TH}) difference of 13.2 V (Figure 4f). Compared with the control device, as shown in Figure 4g–i and Figure S16 (Supporting Information), all the polymer-modified devices exhibited improved TFT performance: the μ_{FE} values were 9 cm^2 V^{-1} s^{-1} for the device with PS, 27 $cm^2V^{-1}s^{-1}$ for that with P3HT, and 53 $cm^2V^{-1}s^{-1}$ for that with TT; the average μ_{FE} values were ∼ approximately 8.83 ± 0.36, 25.21 ± 1.25, and 49.98 ± 2.45 $cm^2V^{-1}s^{-1}$ for the devices with PS,P3HT, and TT, respectively. To our knowledge, the μ_{FE} value of the TT-modified quasi-2D TFT was the highest among those of η = 7 quasi-2D TFTs (Table S3, Supporting Information). To elucidate the TFT performance enhancement effect, we calculated the trap state density (N_{Trap}) using the subthreshold swing (SS) parameter obtained from the TFT transfer curves (Figure 4f–i) (details are given in the Methods section). The N_{Trap} values for each quasi-2D TFT were 0.96 × 10^{12} (control), 0.80 × 10^{12} (with PS), 0.50 × 10^{12} (with P3HT), and 0.55 × 10^{12} (with TT) $cm^{-2}eV^{-1}$. These results indicated that the trap passivation effect of polymer modification contributed to the increased TFT performance with a reduced V_{TH} difference and hysteresis behavior. The hysteresis index (h-index, Figure 4f–i) values were 0.19 for the control device, 0.19 for the device with PS, 0.15 for the device with P3HT, and 0.13 for the device with TT. These improvements were primarily attributed to the passivation of the interfacial traps and mitigation of ion migration within the perovskite semiconductor materials.[48] Notably, the thiophene unit-containing polymer-modified quasi-2D TFTs showed substantial μ_{FE} improvements of approximately four times (with P3HT) and eight times (with TT) compared with that of the control device. These performance-boosting effects also effectively agreed with the corresponding output curve characteristics (Figure 4j–m); the curves showed good linearity at low drain-source voltage (V_{DS}) values and current saturation at high V_{DS} values.

These results suggest that our novel p-doping strategy involving molecular-level (Sn-S) interactions causes an increase in the electronic properties of quasi-2D perovskites and a decrease in the charge-carrier transport barrier at the interface between the perovskite material and gold top electrode; moreover, our results are supported by the decrease in the contact resistance from ≈1000 Ω cm (control and with PS) to ≈750 Ω cm (with P3HT) and 500 Ω cm (with TT) (calculated via the transmission-line method,[49] Figure S17, Supporting Information).

2.4. Device Operational Stability

To explore whether the surface impurity-mediated p-doping affects the stability, we performed operational stability tests on the quasi-2D TFTs without encapsulation under low-vacuum conditions. As shown in **Figure 5a**, the consecutive on/off switching characteristics of the control device showed an off-current decay until 400 s. The TFT device with PS also exhibited a similar current decay phenomenon (Figure S18a, Supporting Information), which originated from the numerous surface trap sites in the quasi-2D perovskite. In contrast, the thiophene-containing polymer-modified TFT samples (P3HT, Figure S18b, Supporting Information; TT, green line in Figure 5a) had a superior consistency in the on/off current states over 1000 cycles. In addition, we investigated the negative bias stress stability in terms of the threshold voltage (V_{TH}) shift while applying a constant gate-source bias voltage (V_{GS} = -40 V). The control device (Figure 5b) and the device with PS (Figure S19a, Supporting Information) showed a significant V_{TH} shift even after the applied bias stress was removed; however, the devices with P3HT (Figure S19b, Supporting Information) and with TT (Figure 5c) had relatively negligible V_{TH} changes and rapidly recovered to their initial performance within 100 s after the bias stress measurements. This result was mainly attributed to the reduced trap density of the quasi-2D perovskites and enhanced carrier transport ability since the V_{TH} shift was strongly related to carrier trapping.[3,17,50]

3. Conclusion

In summary, we introduced a novel surface impurity-mediated p-doping strategy for quasi-2D tin perovskites to enhance their electrical properties. In this study, the incorporation of electronic impurities, specifically thiophene-containing conjugated polymers, onto the top surface of quasi-2D perovskites induced molecular-level Sn-S interactions. This led to a shift in E_F toward the VBM and an increase in both the hole carrier density and the Hall effect mobility. These polymer-modified quasi-2D perovskites exhibited improved surface crystallinity, strain release, and reduced trap states. Additionally, the doped quasi-2D perovskites

the perovskite and TT polymer, and d) corresponding Sobel processed image. e), Sulfur atom mapping of a quasi-2D perovskite film (green region) obtained by EELS, showing the sulfur atoms in the TT polymer (structure in the inset). TFT performance characterization in terms of the transfer f–i) and output j–m) curves: control (black, f and j) and quasi-2D TFTs with PS (blue, g and k), P3HT (red, h and l), and TT (green, i and m). The drain-source voltage (V_{DS}) for transfer curve measurements of TFTs was −40 V, and the hysteresis index (h-index) of the transfer curve (f–i) was calculated as follows: $(\mathcal{P}_{For\rightarrow Rev} - \mathcal{P}_{Rev\rightarrow For})/(\mathcal{P}_{For\rightarrow Rev} + \mathcal{P}_{Rev\rightarrow For})$, where $\mathcal{P}_{For\rightarrow Rev} = \int_{Rev}^{For} |I_{DS}(V)|dV$ and $\mathcal{P}_{Rev\rightarrow For} = \int_{For}^{Rev} |I_{DS}(V)|dV$.

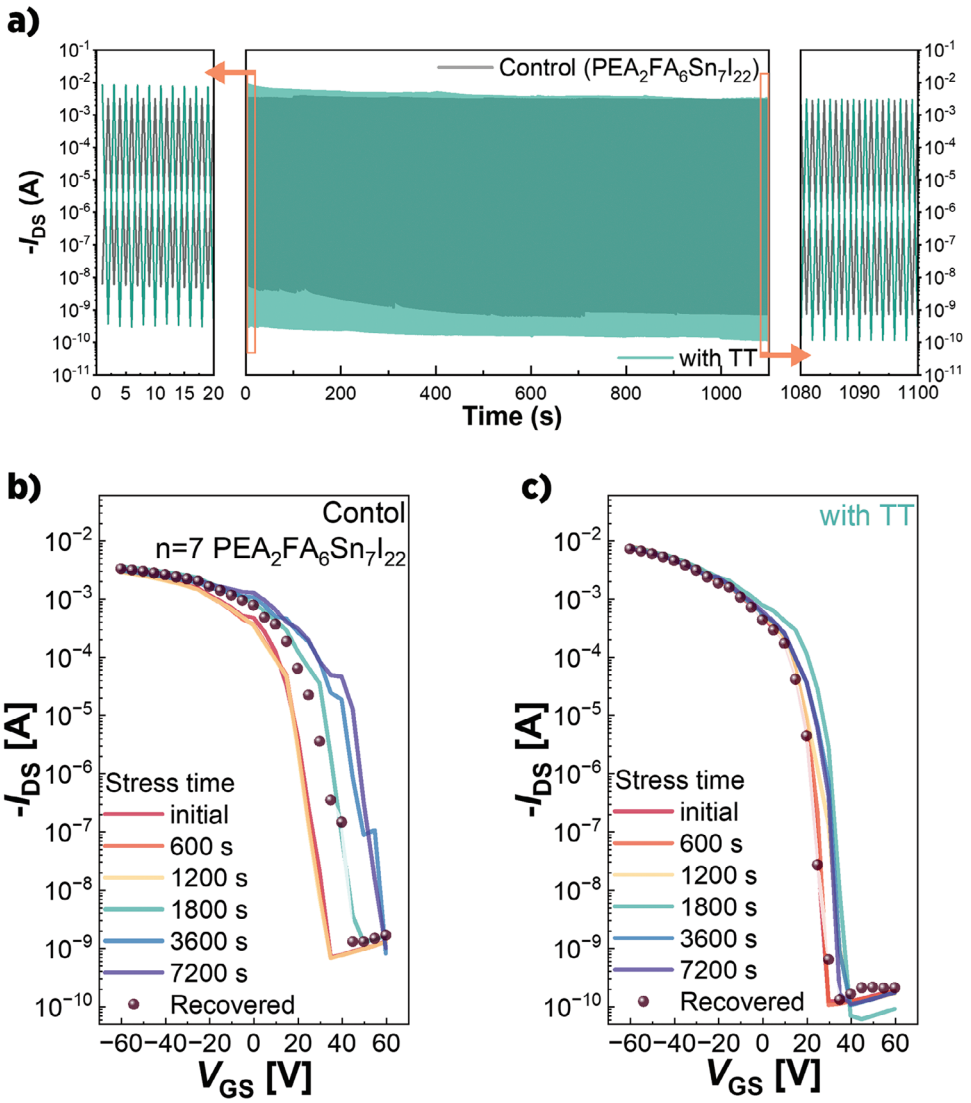

Figure 5. Operational stability tests of the quasi-2D TFT devices. a) Continuous on/off switching sweeps over 1000 cycles ($V_{GS} = \pm 40$ V) for quasi-2D TFTs: control device (black) and device with TT (green). Negative-bias stress tests for various stress durations, and recovery behavior (circles) ($V_{GS} = V_{DS} = -40$ V): b) control device and c) device with TT.

exhibited efficient charge carrier transport ability. With this novel doping strategy, we successfully demonstrated efficient p-type quasi-2D TFTs with a μ_{FE} of 53 $cm^2V^{-1}s^{-1}$, an I_{on}/I_{off} over 10^7, and excellent operational stability. We anticipate that our findings on the surface impurity-mediated p-doping of tin perovskites will provide new insights for the further development of tin perovskite-based optoelectronic device applications.

4. Experimental Section

Materials: Poly[2,5-(2-octyldodecyl)−3,6-diketopyrrolopyrrole-alt-5,5-(2,5-di(thien-2-yl)thieno [3,2-b]thiophene)], [DT-PDPP2T-TT (DPP2T, 1-Materials), TT], Poly(3-hexylthiophene) (P3HT, regio regular electronic grade), and Polystyrene (PS, analytical standard for GPC 100 000) were obtained from 1-Materials, Rieke Metals, and Sigma Aldrich, respectively. Tin (II) iodide (SnI_2) was purchased from Tokyo Chemical Industry (TCI). Phenethylammonium iodide (PEAI, $C_8H_{12}IN$) and formamidinium iodide (FAI, CH_5IN_2) were purchased from Great Cell Solar. A solution of the <n = 7> quasi-2D perovskite precursor, $(PEA)_2(FA)_6Sn_7I_{22}$, was prepared by adding PEAI:FAI:SnI_2 at a molar ratio of 0.2:0.6:0.7 to an anhydrous N,N-dimethylformamide (DMF, Sigma–Aldrich)/dimethyl sulfoxide (DMSO, Sigma–Aldrich) mixed solution (4:1 volume ratio) with 20 mmol (0.1 molar ratio of tin) tin (II) fluoride (SnF_2, Sigma Aldrich) to suppress oxidization of the tin (II) ions. All chemicals were used without pretreatment.

Device Fabrication: The top-contact bottom-gate structured quasi-2D perovskite-based thin film transistors (quasi-2D TFTs) were fabricated with the following configuration: Si/SiO_2/quasi-2D perovskite/optional polymer material (PS, P3HT, or TT)/Au. To deposit the quasi-2D perovskite materials, UV-ozone-treated Si/SiO_2 substrates were transferred into an N_2-filled glove box. The quasi-2D perovskite layers were spin-cast at 5000 rpm for 60 s on the SiO_2 substrates. During spin-casting (after 15 s), the quasi-2D perovskite layer was treated with 150 µL of chlorobenzene (CB, Sigma-Aldrich) using the antisolvent treatment method. Subsequently, the quasi-2D perovskite films were thermally annealed at 100 °C for 7 min. Afterward,

to fabricate the optional polymer layer, each polymer solution (various concentrations in CB) was drop-cast on top of the quasi-2D perovskite films at 4000 rpm for 30 s, followed by annealing at 100 °C for 1 min to remove the residual solvent. Finally, 70 nm-thick Au source-drain electrodes were deposited using a thermal evaporation process under high-vacuum conditions (1×10^{-6} Torr).

Characterization—Transient Absorption Spectroscopy Measurements: Femtosecond transient absorption (TA) spectra and decays were acquired using a custom-made TA spectrometer consisting of a femtosecond Ti:sapphire regenerative amplifier system (Hurricane, Spectra Physics) and a multichannel spectrometer (Ocean FX and NIR Quest, Ocean Insight). A pump pulse at 400 nm was generated with a power density of ~1 μJ/cm^2 using an optical parametric amplifier (IR-OPA, Spectra-Physics) and a neutral density filter, while a broadband white-light continuum probe pulse was generated by focusing a small portion of the 800 nm amplifier output into a sapphire window. TA signals as a function of delay time were collected using an optical fiber coupled with multichannel spectrometers from Ocean Insight (Ocean FX and NIR Quest). More details on the custom-made TA system were given in a previous publication.[51,52] The steady-state fluorescence spectra were measured using a custom-made fluorescence spectrophotometer (QE-Pro, Ocean Insight). The time-resolved fluorescence-decay profiles were recorded using a time-correlated single photon counting (TCSPC) system combined with a picosecond laser (LDH-P-C-470, PicoQuant), a monochromator (SP-2150, Princeton Instruments), a multichannel plate photomultiplier tube (R3809U-51, Hamamatsu), and a photon counting module (**SPC-130-EM**, Becker & Hickl GmbH). The PL decay time constants were obtained by fitting with a multiexponential function, i.e., $I(t) = A_1\exp(-t/\tau_1) + A_2\exp(-t/\tau_2)$, where I(t) is the time-dependent PL intensity, A is the normalized amplitude, and τ is the fitted PL lifetime. The average decay times were obtained using $(A_1\tau_1 + A_2\tau_2)/(A_1 + A_2)$.

Characterization—PL Lifetime Mapping Measurements: For PL lifetime mapping, a time-resolved photoluminescence (TRPL) study was carried out using a confocal microscope (MicroTime-200, Picoquant, Germany) with a 40 × (air) objective. Lifetime measurements were performed at the Korea Basic Science Institute (KBSI), Daegu Center, Korea. A single-mode pulsed diode laser (470 nm with a pulse width of ~30 ps and an average power of ≈100 nW operating at a 5 MHz repetition rate) was used as an excitation source. A dichroic mirror (490 DCXR, AHF), a long-pass filter (HQ500lp, AHF), a 100 μm pinhole, a bandpass filter (550 ± 20, 650 ± 20, or 850 ± 20 nm; Thorlabs), and a single photon avalanche diode (PDM series, MPD) were used to collect emission from the samples. A time-correlated single-photon counting system (PicoHarp-300, PicoQuant GmbH, Germany) was used to count the emission photons. PL lifetime images consisting of 250 × 250 pixels were recorded using the time-tagged time-resolved (TTTR) data acquisition method. Exponential function fittings for the obtained PL decays were performed using Symphotime-64 software (Ver. 2.2). All samples for the photoluminescence analysis were encapsulated by the cover glass with UV epoxy agents to suppress the oxidization of the tin-based perovskite materials.

Characterization—UV–vis Absorption and FT-IR Measurements: UV–vis-NIR absorption spectra were obtained using a UV–vis-NIR spectrophotometer (Cary 5000 UV–vis-NIR, Agilent Technologies, Inc.). IR transmittance spectra were collected with an FT-IR spectrometer (VERTEX 70, Bruker Co., Ltd.) using a zinc selenide (ZnSe) substrate under a N_2 atmosphere.

Characterization—Thin Film Characterization: High-resolution grazing angle X-ray diffraction (GIXRD) patterns were collected using a SmartLab diffractometer (Rigaku). Photoelectron spectroscopy was carried out using a NEXSA system (Thermo Fisher Scientific) with He (I) radiation (21.22 eV) and Al Kα radiation for the UPS and XPS measurements, respectively. The GIXRD and photoelectron spectroscopy samples were analyzed using their respective sample holders (Rigaku, Thermo Fisher Scientific) under protective atmospheres to prevent oxygen from affecting the perovskite materials. SEM and HAADF-STEM images were captured with a Regulus 8100 (Hitachi High-Tech Group) and a JEM-ARM300F2 (JEOL, USA), respectively, under high vacuum conditions. These thin-film characterizations were performed at the GIST Advanced Institute of Instrumental Analysis (GAIA).

Characterization—AFM and Hall Effect Measurements: AFM analysis of the perovskite film was performed using an XE-100 microscope (Park System, South Korea). An HL5500PC instrument (Accent Optical Technologies, USA) was used for Hall effect measurements. The samples used for the Hall effect measurements were prepared with the following structure: glass substrate/perovskite/gold electrode as the contact electrode.

Characterization—Electrical Measurements: The current–voltage (*I--V*) characteristics of the quasi-2D TFTs were measured using a Keithley 4200 source meter under low vacuum conditions (1×10^{-2} Torr). The field-effect mobility(μ_{FE})of the quasi-2D TFTs was calculated using the following equation: $\mu_{FE} = (2L/WC_i)(\partial\sqrt{I_{DS}}/\partial V_{GS})^2$, where I_{DS} and V_{GS} are the drain-source current and gate-source voltage, respectively; L is the channel length (100 μm); W is the channel width (1000 μm); and C_i is the capacitance per unit area of the gate dielectric layer (C_i = 11.5 nF·cm^{-2} for a SiO_2 dielectric layer with a thickness of 300 nm). The subthreshold swing (*SS*) was obtained from the inverse of the maximum slope of the I_{DS}-V_{GS} plot. The trap density (N_{trap}) of the quasi-2D TFTs was calculated using the formula $N_{trap} = [SSqlog(e)/kT - 1](C_i/q)$, where *q* and k are the charges of the electron and the Boltzmann constant, respectively, and *e* is the base of the natural logarithm.[17]

Supporting Information

Supporting Information is available from the Wiley Online Library or from the author.

Acknowledgements

J.-H.K. would like to thank the Heeger Center for Advanced Materials (HCAM) at the Gwangju Institute of Science and Technology (GIST) for assisting with device fabrication and analysis. This work was supported by the National Research Foundation of Korea (NRF) grant funded by the Korean government (MSIT) (No. 2020R1A2C3003653, RS-2024-00333515); by the Technology Development Program to Solve Climate Change of the NRF funded by MSIT (NRF-2020M1A2A2080748); and by the GIST Research Institute (GRI, APRI) via a grant funded by the GIST in 2024.

Conflict of Interest

The authors declare no conflict of interest.

Data Availability Statement

The data that support the findings of this study are available from the corresponding author upon reasonable request.

Keywords

2D perovskite, charge transport, field-effect transistor, organic-inorganic hybrid material, p-doing

Received: July 18, 2024
Revised: August 13, 2024
Published online: August 29, 2024

[1] R. A. John, Y. Demirağ, Y. Shynkarenko, Y. Berezovska, N. Ohannessian, M. Payvand, P. Zeng, M. I. Bodnarchuk, F. Krumeich, G. Kara, I. Shorubalko, M. V. Nair, G. A. Cooke, T. Lippert, G. Indiveri, M. V. Kovalenko, *Nat. Commun.* **2022**, *13*, 2074.

[2] A. E. K. Kaplan, C. J. Krajewska, A. H. Proppe, W. Sun, T. Sverko, D. B. Berkinsky, H. Utzat, M. G. Bawendi, *Nat. Photonics* **2023**, *17*, 775.
[3] A. Liu, H. Zhu, S. Bai, Y. Reo, M. Caironi, A. Petrozza, L. Dou, Y.-Y. Noh, *Nat. Electron.* **2023**, *6*, 559.
[4] D. B. Mitzi, C. A. Feild, W. T. A. Harrison, A. M. Guloy, *Nature* **1994**, *369*, 467.
[5] K. X. Steirer, P. Schulz, G. Teeter, V. Stevanovic, M. Yang, K. Zhu, J. J. Berry, *ACS Energy Lett.* **2016**, *1*, 360.
[6] L. M. Herz, A. C. S. Energy Letters, **2017**, *2*, 1539.
[7] C. C. Stoumpos, C. D. Malliakas, M. G. Kanatzidis, *Inorg. Chem.* **2013**, *52*, 9019.
[8] L. Lanzetta, T. Webb, J. M. Marin-Beloqui, T. J. Macdonald, S. A. Haque, *Angew. Chem., Int. Ed.* **2023**, *62*, 202213966.
[9] W.-F. Yang, F. Igbari, Y.-H. Lou, Z.-K. Wang, L.-S. Liao, *Adv. Energy Mater.* **2020**, *10*, 1902584.
[10] D. Ricciarelli, D. Meggiolaro, F. Ambrosio, F. De Angelis, *ACS Energy Lett.* **2020**, *5*, 2787.
[11] L. Yan, J. Ma, P. Li, S. Zang, L. Han, Y. Zhang, Y. Song, *Adv. Mater.* **2022**, *34*, 2106822.
[12] L. N. Quan, M. Yuan, R. Comin, O. Voznyy, E. M. Beauregard, S. Hoogland, A. Buin, A. R. Kirmani, K. Zhao, A. Amassian, D. H. Kim, E. H. Sargent, *J. Am. Chem. Soc.* **2016**, *138*, 2649.
[13] L. Mao, C. C. Stoumpos, M. G. Kanatzidis, *J. Am. Chem. Soc.* **2019**, *141*, 1171.
[14] J. C. Blancon, A. V. Stier, H. Tsai, W. Nie, C. C. Stoumpos, B. Traoré, L. Pedesseau, M. Kepenekian, F. Katsutani, G. T. Noe, J. Kono, S. Tretiak, S. A. Crooker, C. Katan, M. G. Kanatzidis, J. J. Crochet, J. Even, A. D. Mohite, *Nat. Commun.* **2018**, *9*, 2254.
[15] H. Tsai, W. Nie, J. C. Blancon, C. C. Stoumpos, R. Asadpour, B. Harutyunyan, A. J. Neukirch, R. Verduzco, J. J. Crochet, S. Tretiak, L. Pedesseau, J. Even, M. A. Alam, G. Gupta, J. Lou, P. M. Ajayan, M. J. Bedzyk, M. G. Kanatzidis, *Nature* **2016**, *536*, 312.
[16] Y. Reo, T. Choi, J.-Y. Go, S. Jeon, B. Lim, H. Zhu, A. Liu, Y.-Y. Noh, *ACS Energy Lett.* **2023**, *8*, 3088.
[17] A. Liu, H. Zhu, S. Bai, Y. Reo, T. Zou, M.-G. Kim, Y.-Y. Noh, *Nat. Electron.* **2022**, *5*, 78.
[18] H. Zheng, G. Liu, L. Zhu, J. Ye, X. Zhang, A. Alsaedi, T. Hayat, X. Pan, S. Dai, *Adv. Energy Mater.* **2018**, *8*, 1800051.
[19] Y. Chen, S. Yu, Y. Sun, Z. Liang, *J. Phys. Chem. Lett.* **2018**, *9*, 2627.
[20] J. Kim, Y. S. Shiah, K. Sim, S. Iimura, K. Abe, M. Tsuji, M. Sasase, H. Hosono, *Adv. Sci. (Weinh)* **2022**, *9*, 2104993.
[21] L. Yan, J. Ma, P. Li, S. Zang, L. Han, Y. Zhang, Y. Song, *Adv. Mater.* **2022**, *34*, 2106822.
[22] W. E. Spear, P. G. Le Comber, *Solid State Commun.* **1975**, *17*, 1193.
[23] R. A. Street, *Phys. Rev. Lett.* **1982**, *49*, 1187.
[24] P. M. Fahey, P. B. Griffin, J. D. Plummer, *Rev. Mod. Phys.* **1989**, *61*, 289.
[25] A. Liu, R. Jones, L. Liao, D. Samara-Rubio, D. Rubin, O. Cohen, R. Nicolaescu, M. Paniccia, *Nature* **2004**, *427*, 615.
[26] N. Shrestha, Z. Song, C. Chen, E. Bastola, X. Wang, Y. Yan, R. J. Ellingson, *J. Phys. Chem. Lett.* **2020**, *11*, 121.
[27] H. Yan, B. Wang, X. Yan, Q. Guan, H. Chen, Z. Shu, D. Wen, Y. Cai, *Materials Today Energy* **2022**, *27*, 101038.
[28] M. A. Haque, T. Zhu, L. H. Hernandez, R. Tounesi, C. Combe, B. Davaasuren, A.-H. Emwas, F. P. García de Arquer, E. H. Sargent, D. Baran, *Cell Reports Physical Science* **2023**, 4.
[29] L. Lanzetta, L. Gregori, L. H. Hernandez, A. Sharma, S. Kern, A. M. Kotowska, A.-H. Emwas, L. Gutiérrez-Arzaluz, D. J. Scurr, M. Piggott, D. Meggiolaro, M. A. Haque, F. De Angelis, D. Baran, *ACS Energy Lett.* **2023**, *8*, 2858.
[30] A. Nebatti Ech-Chergui, P. R. Ghediya, Y. Khane, M. Guezzoul, A. Popa, A. S. Kadari, M. Adjdir, K. Kesavan, D. J. Lockwood, K. D. Khodja, B. Amrani, A. Zekri, B. Aïssa, *Phys. B* **2023**, 667.
[31] A. Rafie, R. Pereira, A. A. Shamsabadi, V. Kalra, *J. Phys. Chem. C* **2022**, *126*, 12327.
[32] G. Rajendra Kumar, A. Dennyson Savariraj, S. N. Karthick, S. Selvam, B. Balamuralitharan, H. J. Kim, K. K. Viswanathan, M. Vijaykumar, K. Prabakar, *Phys. Chem. Chem. Phys.* **2016**, *18*, 7284.
[33] Y. J. Heo, H. J. Jang, J.-H. Lee, S. B. Jo, S. Kim, D. H. Ho, S. J. Kwon, K. Kim, I. Jeon, J.-M. Myoung, J. Y. Lee, J.-W. Lee, J. H. Cho, *Adv. Funct. Mater.* **2021**, *31*, 2106974.
[34] A. Telfah, M. A. Al-Akhras, K. A. Al-Izzy, A. A. Ahmad, R. Ababneh, M. J. A. Ahmad, C. J. Tavares, R. Hergenröder, *Polym. Bull.* **2022**, *79*, 3759.
[35] Y. Su, J. Yang, G. Liu, W. Sheng, J. Zhang, Y. Zhong, L. Tan, Y. Chen, *Adv. Funct. Mater.* **2022**, *32*, 2109631.
[36] H. Liu, Z. You, S. Yang, C. Liu, X. Xie, K. Xiang, X. Wang, X. Yan, *Environ. Sci. Pollut. Res.* **2019**, *26*, 6735.
[37] S. I. Kudryashov, L. V. Nguyen, D. A. Kirilenko, P. N. Brunkov, A. A. Rudenko, N. I. Busleev, A. L. Shakhmin, A. V. Semencha, R. A. Khmelnitsky, N. N. Melnik, I. N. Saraeva, A. A. Nastulyavichus, A. A. Ionin, E. R. Tolordava, Y. M. Romanova, *ACS Appl. Nano Mater.* **2018**, *1*, 2461.
[38] D. M. Hausmann, R. G. Gordon, *J. Cryst. Growth* **2003**, *249*, 251.
[39] S. Sidhik, Y. Wang, M. De Siena, R. Asadpour, A. J. Torma, T. Terlier, K. Ho, W. Li, A. B. Puthirath, X. Shuai, A. Agrawal, B. Traore, M. Jones, R. Giridharagopal, P. M. Ajayan, J. Strzalka, D. S. Ginger, C. Katan, M. A. Alam, J. Even, M. G. Kanatzidis, A. D. Mohite, *Science* **2022**, *377*, 1425.
[40] N. Zhou, Y. Shen, L. Li, S. Tan, N. Liu, G. Zheng, Q. Chen, H. Zhou, *J. Am. Chem. Soc.* **2018**, *140*, 459.
[41] C. Zhu, X. Niu, Y. Fu, N. Li, C. Hu, Y. Chen, X. He, G. Na, P. Liu, H. Zai, Y. Ge, Y. Lu, X. Ke, Y. Bai, S. Yang, P. Chen, Y. Li, M. Sui, L. Zhang, H. Zhou, Q. Chen, *Nat. Commun.* **2019**, *10*, 815.
[42] D. Liu, D. Luo, A. N. Iqbal, K. W. P. Orr, T. A. S. Doherty, Z.-H. Lu, S. D. Stranks, W. Zhang, *Nat. Mater.* **2021**, *20*, 1337.
[43] N. R. Yogamalar, A. C. Bose, *Appl. Phys. A* **2011**, *103*, 33.
[44] B. Yang, D. Bogachuk, J. Suo, L. Wagner, H. Kim, J. Lim, A. Hinsch, G. Boschloo, M. K. Nazeeruddin, A. Hagfeldt, *Chem. Soc. Rev.* **2022**, *51*, 7509.
[45] D. Shi, V. Adinolfi, R. Comin, M. Yuan, E. Alarousu, A. Buin, Y. Chen, S. Hoogland, A. Rothenberger, K. Katsiev, Y. Losovyj, X. Zhang, P. A. Dowben, O. F. Mohammed, E. H. Sargent, O. M. Bakr, *Science* **2015**, *347*, 519.
[46] L. Kong, X. Zhang, Y. Li, H. Wang, Y. Jiang, S. Wang, M. You, C. Zhang, T. Zhang, S. V. Kershaw, W. Zheng, Y. Yang, Q. Lin, M. Yuan, A. L. Rogach, X. Yang, *Nat. Commun.* **2021**, *12*, 1246.
[47] N. Kanopoulos, N. Vasanthavada, R. L. Baker, *IEEE Journal of Solid-State Circuits* **1988**, *23*, 358.
[48] P. Cheng, G. Liu, X. Dong, Y. Zhou, C. Ran, Z. Wu, *ACS Applied Electronic Materials* **2024**, *6*, 3039.
[49] Y. Xu, R. Gwoziecki, I. Chartier, R. Coppard, F. Balestra, G. Ghibaudo, *Appl. Phys. Lett.* **2010**, *97*, 063302.
[50] Y.-H. Lin, W. Li, H. Faber, A. Seitkhan, N. A. Hastas, D. Khim, Q. Zhang, X. Zhang, N. Pliatsikas, L. Tsetseris, P. A. Patsalas, D. D. C. Bradley, W. Huang, T. D. Anthopoulos, *Nat. Electron.* **2019**, *2*, 587.
[51] C.-M. Oh, J. Lee, S. H. Park, I.-W. Hwang, *Spectrochim. Acta, Part A* **2021**, *250*, 119227.
[52] C.-M. Oh, J. Lee, S. H. Park, I.-W. Hwang, *J. Phys. Chem. Lett.* **2021**, *12*, 6418.